Nanoscale Measurements of Elastic Properties and Hydrostatic Pressure in H$_2$-Bulged MoS$_2$ Membranes

Cinzia Di Giorgio, Elena Blundo, Giorgio Pettinari, Marco Felici, Yuerui Lu, Anna Maria Cucolo, Antonio Polimeni, and Fabrizio Bobba*

The combination of extremely high stiffness and bending flexibility with tunable electrical and optical properties makes van der Waals transition metal dichalcogenides appealing both for fundamental science and applied research. By taking advantage of localized H$_2$-bulged MoS$_2$ membranes, an innovative approach, based on atomic force microscopy nanoindentation, is demostrated and discussed here, aiming at measuring elastic and thermodynamic properties of nanoblisters made of 2D materials. The results, interpreted in the membrane limit of the Föppl–von Karman equation, lead to the quantification of the internal pressure and mole number of the trapped H$_2$ gas, as well as of the stretching modulus and adhesion energy of the MoS$_2$ membrane. The latter is discussed in the limit of strong (clamped and fully bonded interlayer interface) shear, as experimentally achieved in the investigated H$_2$-bulged 2D blisters. Moreover, this approach allows to quantify the stress, and consequently the strain, locally imposed to the MoS$_2$ membrane by the bulging of the domes.

1. Introduction

Molybdenum disulfide (MoS$_2$) is a 2D layered crystal consisting of stacked S-Mo-S sheets, with strong in-plane covalent bonds between Mo and S atoms and weak van der Waals interaction holding the layers together, thus enabling the isolation of single or few layers, akin to graphene.[1] As a wide bandgap semiconductor (1.9 eV at room temperature in the monolayer form),[2] MoS$_2$ has easily found possible applications in electronic and optoelectronic devices.[3–5] Moreover, it has attracted growing interest due to the great tunability of its electronic properties as a function of layer thickness,[2,6–8] strain,[9–13] defects, and intercalations,[14–18] charge carrier doping,[19–21] charge transfer,[22,23] and pressure.[24] In addition to this, due to its intrinsic atomically smooth surface, it has been regarded as an ideal barrier for tunneling junctions.[25] Single-layer MoS$_2$ has been theoretically predicted to withstand a critical intrinsic stress and strain of $\sigma_c \approx$ 24GPa and $\varepsilon_c \approx$ 20% for biaxial tensile deformations (and higher for uniaxial), by employing first-principle calculations and investigating the stress–strain ($\sigma - \varepsilon$) relations up to the failure point.[26,27] On the other hand, experimental estimates of ε_c in MoS$_2$ sheets subjected to nanoindentation (which has the effect of a biaxial tensile stress), lead to lower values, $\varepsilon_c =$ 6%—13%,[27,28] for measured σ_c close to the expected one. The discrepancy in the experimental value of ε_c is caused by the use of a linear $\sigma - \varepsilon$ relation, $\sigma = Y\varepsilon$, where Y is the material Young's modulus, in a no-longer linear regime (close to the breaking point).

Recently, the excellent robustness and flexibility of MoS$_2$ and other 2D crystals has led to a keen interest into 2D-material-blisters, such as bubbles, wrinkles, and tents. Their spontaneous formation has been observed after transferring 2D materials on top of a substrate, or on stacks of van der Waals (vdW) heterostructures, and it has been attributed to the trapping of adsorbed water and/or hydrocarbons inevitably present on the individual layers before assembly.[29–31] Moreover,

Dr. C. Di Giorgio, Prof. A. M. Cucolo, Prof. F. Bobba
Department of Physics E.R: Caianiello
University of Salerno
Fisciano 84084, Italy
E-mail: fbobba@unisa.it

Dr. C. Di Giorgio, Prof. F. Bobba
INFN
Sezione di Napoli
Gruppo Collegato di Salerno
Complesso Universitario di Monte S. Angelo
Napoli 80126, Italy

E. Blundo, Prof. M. Felici, Prof. A. Polimeni
Physics Department
Sapienza University of Rome
Rome 00185, Italy

Dr. G. Pettinari
Institute for Photonics and Nanotechnologies
National Research Council
Rome 00156, Italy

Prof. Y. Lu
Research School of Electrical
Energy and Materials Engineering
College of Engineering and Computer Science
The Australian National University
Canberra ACT2601, Australia

Prof. F. Bobba
CNR-SPIN
Fisciano, SA 84084, Italy

**ADVANCED
SCIENCE NEWS**
www.advancedsciencenews.com

**ADVANCED
MATERIALS
INTERFACES**
www.advmatinterfaces.de

several strategies for artificially inducing nanoblistering in 2D materials have been developed and employed, such as surface etching,[32,33] low temperature growth,[34,35] and surface hydrogenation.[36–40]

The growing interest into 2D material blisters relies on the possibility of using them as a tool to probe and study: 1) the induced strain occurring at the blister surface and its impact on the electronic and optical properties of 2D materials; 2) the elastic properties of the 2D crystal involved (stretching modulus, Young's modulus, adhesion and/or exfoliation energy); 3) the nanoscale confinement exerted on the enclosed material (e.g., hydrostatic pressure). These studies are particularly relevant for the field of straintronics and twistronics (e.g., applications of flexible and stretchable electronics and photonics based on 2D materials and vdW heterostructures). Recently, several groups demonstrated the ability to investigate the elastic properties of 2D materials at the nanoscale, by atomic force microscopy (AFM) nanoindentation on free-standing membranes obtained by suspending mono- or few-layers of 2D crystals on top of microcavities,[27,41–45] by bimodal AFM on monolayers,[46] or even by combining AFM and high spatial resolution Raman spectroscopy.[47] However, the quest for the measurement of the adhesion energy between a monolayer of 2D material and its substrate (or exfoliation energy between the layers of a 2D crystal) has further motivated the development of experiments on the delamination of monolayers from the substrate (e.g., by a controlled pressurization of monolayers through the microcavities of a holey substrate,[48,49] or by the intercalation of nanoparticles to generate blisters on the substrate surface [50]), as well as theoretical efforts to describe the problem and relate the shape and aspect ratio of the blisters to their elastic and thermodynamic properties (stretching modulus, adhesion energy, and inner gas pressure).[51–54]

In this paper, we report a novel approach for a systematic measurement of inner gas pressure, membrane stretching modulus, crystal exfoliation energy and strain in blisters made of 2D materials. We expose mechanically exfoliated MoS_2 bulk flakes to hydrogen ion irradiations[39] to intentionally induce the formation of hydrogen-filled, nano- and micro-sized spherical membranes (spontaneously formed domes), holding a large, local biaxial strain. The formation process is also engineered, allowing the creation of ordered arrays of domes, clamped at their edges and containing over-pressurized gas (engineered clamped domes).[40] The loading resistance of these structures is probed by AFM nanoindentation experiments, and the results are compared to the solutions of the Föppl–von Karman equation,[53,54] describing the mechanics of thin plates under large deformations.

Here, we use the Föppl–von Karman approach by introducing some novelty elements: first, we apply the macroscopic elastic model to the relatively new context of nanoscale deformations of ultrathin shells of 2D materials (MoS_2 bulged domes).[55–57] Second, we consider a modified formulation of the Föppl–von Karman equation (in the membrane limit), including the action of two loading forces: the internal gas pressure and the local indentation force.[54,57] Finally, we apply the Föppl–von Karman theoretical formulation to interpret the findings of AFM nanoindentation experiments on two different systems, i.e., the spontaneously formed and the engineered clamped domes.

This work leads to multiple outcomes: on one side the precise knowledge of the amount of hydrogen molecules confined in the domes, together with the technological capability of producing domes in a controlled manner, has applicative potentialities. For instance, it can be exploited for the on-demand delivery of extremely small quantities of reactive gas, useful for nanoreactors[58] and for fine calibration kits for H_2 sensors. It is worth mentioning that a one-by-one membrane breaking, with consequent gas release, can be induced, for example, by a properly focused laser scanning over the crystal surface (a movie showing this procedure is presented as supplementary material). On the other side, the measurement of stretching modulus, stress/strain, and adhesion energy allows for a full characterization of the 2D crystal's elastic properties. In this framework, the results of our loading experiments point toward a fine tuning of the mechano-elastic properties of MoS_2 domes: compared to the spontaneously formed MoS_2 membranes, the engineered domes exhibit higher level of strain,[40] stiffer behavior to the AFM solicitation—up to 500 nN—and higher internal pressure and exfoliation energy. We discuss these findings as a consequence of the superimposed constraint, acting as a source of strong clamping at the interface between the topmost layer and the bulk, and preventing local delamination of the MoS_2 layer at the edge of the dome.

2. Results and Discussions

2.1. Membrane Formation in MoS_2

Localized protrusions, or domes, have been obtained in MoS_2 bulk flakes via hydrogen ion irradiation: it has been recently demonstrated that accelerated protons possess enough kinetic energy to penetrate through MoS_2 (as well as other transition-metal dichalcogenides, graphene and h-BN) planes, without damaging the crystal lattice. The subsequent formation of hydrogen molecules in the crystal interlayer regions gives rise to localized protrusions appearing on the flake surface in the shape of domes.[36–40] Here, we engineer the dome formation process as follows:[40] first of all, MoS_2 flakes are mechanically exfoliated onto a Si/SiO$_2$ substrate (top panel of **Figure 1**a); subsequently, the sample is partially coated by hydrogen silsesquioxane (HSQ) negative-tone e-beam resists, of thickness varying in the range 50–100 nm; then, octagonal openings of micrometer-scale radius (middle panel of Figure 1a) are created in the HSQ layer via electron-beam lithography (EBL); finally, a low-energy proton irradiation is performed (bottom panel of Figure 1a). Additional information on sample production, patterning, and irradiation is reported in the Experimental Section. Uncoated MoS_2 flakes reveal the formation of randomly distributed domes of random size (sponeously formed), whereas in the patterned flakes the domes can form only within the openings. With this method, a regular array of domes with uniform size distribution can be achieved by controlling the area of the sample participating in the hydrogen production process. Figure 1b,c compare tapping-mode AFM topographies, 15 µm × 15 µm in lateral size, of uncoated and HSQ-coated MoS_2 surfaces, revealing the evolution toward a fine control of dome size and position due to the engineering of the sample
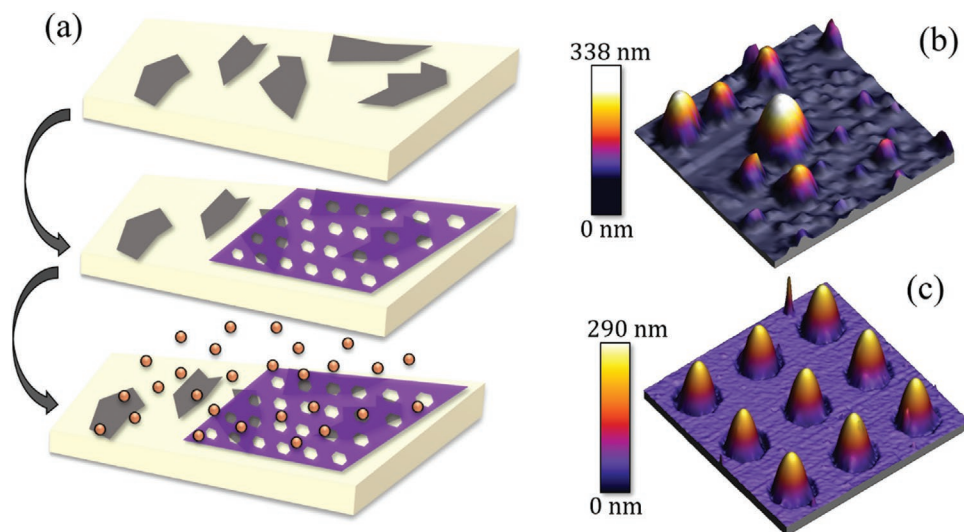
Figure 1. a) Schematic illustration of the process used to achieve spontaneous and ordered domes. Top panel: MoS$_2$ flakes are mechanically exfoliated on top of a Si/SiO$_2$ substrate. Middle panel: the substrate is partially coated by hydrogen silesquioxane (HSQ) negative-tone e-beam resists, with octagonal openings of micrometer-scale radius. Bottom panel: low energy proton irradiation is performed. b) Tapping-mode AFM topography of uncoated MoS$_2$ surface after proton irradiation, 15 µm × 15 µm in lateral size. c) Tapping-mode AFM topography of HSQ-MoS2 surface after proton irradiation, 15 µm × 15 µm in lateral size.

prior to H$^+$ irradiation (corresponding optical images are given in Note S1 in the Supporting Information). Furthermore, the spontaneously created domes have a typical aspect ratio $h/R = 0.16$ (where h is the maximum height and R the footprint radius of the dome), namely universal value, in agreement with previous measurements;[29,39,40] on the contrary, the presence of the HSQ mask favors an over-pressurization of the internal gas inside the engineered domes, making their aspect ratio higher than 0.16.[40] With this method we have thus intentionally created domes spanning over a wide range of aspect ratios in between 0.15 and 0.31, thus permitting studies under quite different conditions, otherwise unattainable.

More specifically, in this work we have focused on three different sizes for the HSQ openings (and consequently for the MoS$_2$ domes): 5, 3, and 1.2 µm in diameter, hereinafter referred to as big, medium, and small size.

The AFM topographies of **Figure 2**a–c compare the nucleation of H$_2$-filled domes, as obtained by reducing the opening size (from 5 to 1.2 µm) and pattern periodicity (an AFM image of the corresponding HSQ mask is given in Note S1 in the Supporting Information). The AFM scan size scales from 15 µm × 15 µm in (a), to 9 µm × 9 µm in (b), to 5.5 µm × 5.5 µm in (c), whereas the height range (from dark blue to yellow) is 495, 330, and 150 nm in (a), (b), and (c), respectively. Figure 2d zooms in on a small dome, protruding from a 50-nm thick and 1.2-µm wide HSQ-opening. The dome profile overlays to the AFM image, revealing a maximum height and radius of $h = 138$ nm and $R = 520$ nm, respectively. This leads to an aspect ratio of $h/R = 0.265$, remarkably higher than the universal value $h/R = 0.16$.[29,40]

2.2. Nanoscale Measure of Inner Pressure and Elastic Properties

We performed AFM nanoindentation to measure the H$_2$ pressure inside the domes and the relevant elastic and adhesion

parameters of the 2D MoS$_2$ membranes. A similar approach has been used in the past to measure osmotic pressure inside viral particles,[59] pressurized elastic shells of finite thickness,[60] as well as bubbles generated by transferring monolayers of 2D materials.[29,57]

Here, we take a systematic approach using the membrane limit of the Föppl–von Karman equation in the case of indentation on pressurized ultrathin elastic sheets, clamped to the edge of a circular hole of footprint radius R.[54] In particular, Föppl and von Karman wrote a system of coupled, nonlinear, partial differential equations, establishing the relation between the following quantities: deflection of the plate, stress, Young's modulus of the material Y, geometrical dimensions of the plate (lateral size and thickness t), applied load, and flexural rigidity $D = \frac{Yt^3}{12(1-v^2)}$ (where v is the Poisson ratio of the material).[61,62] As the thickness t approaches zero (membrane limit), the flexural rigidity, and consequently the bending stiffness, becomes negligible (more information is given in Note S2 in the Supporting Information). By modeling the AFM sharp tip as a finite indenter of radius $R_{tip} \ll R$, exerting a normal load on the top of the pressurized domes, the problem of indentation on the clamped, pressurized and pre-tensed membrane can be written by incorporating the differential pressure $\Delta p = p - p_0$, with p and p_0 internal and external pressure respectively, in the normal force balance equation

$$\psi(r)\frac{d\zeta}{dr} = \frac{F}{2\pi} - \frac{\Delta p}{2}r^2 \tag{1}$$

where $\psi(r)$ is the Airy stress function, related to the radial and circumferential stress components as $\sigma_{rr} = \psi/r$ and $\sigma_{\theta\theta} = d\psi/dr$, respectively, and $\zeta(r)$ is the out-of-plane membrane displacement due to the simultaneous action of indentation force F and differential pressure $\Delta p = p - p_0$. This equation can be solved numerically, together with the strain compatibility equation,
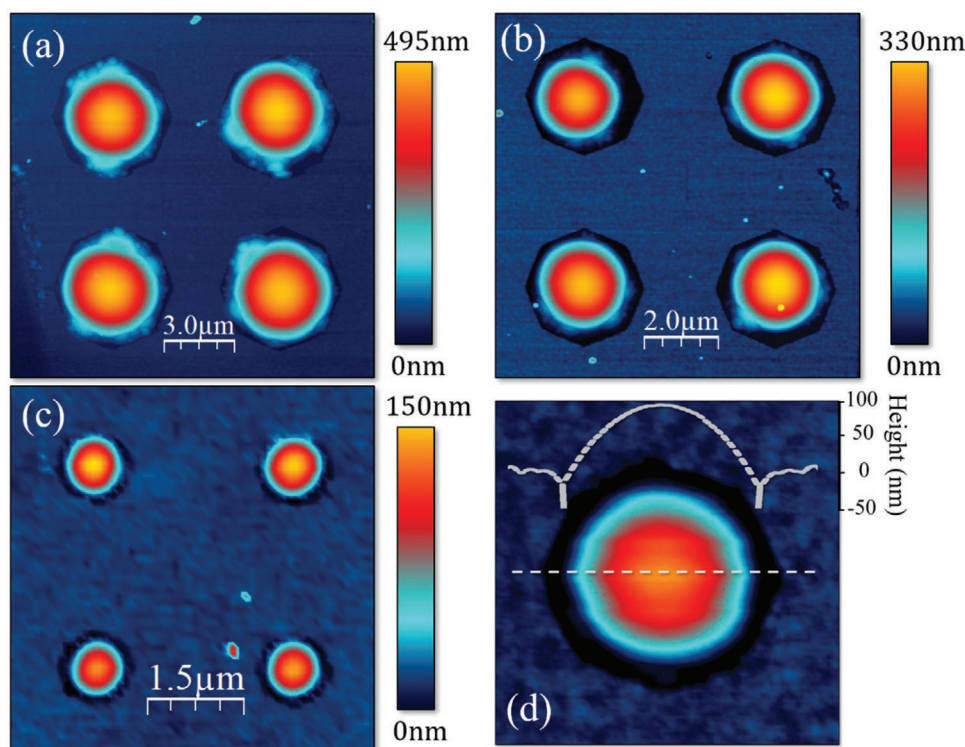
Figure 2. Tapping-mode AFM topography of a) big domes—scan size is 15 µm × 15 µm; b) medium domes—scan size is 9 µm x 9 µm; c) small domes—scan size is 5.5 µm × 5.5 µm. d) Tapping-mode AFM topography of a small dome—scan size is 1.9 µm × 1.9 µm with overlaid height profile.

which sets the unique relation between the stress and the out-of-plane displacement, through the stretching modulus, or 2D Young's modulus, E_{2D}

$$r \frac{d}{dr} \left[\frac{1}{r} \frac{d}{dr} r \psi \right] = -\frac{1}{2} E_{2D} \left(\frac{d\zeta}{dr} \right)^2 \quad (2)$$

with boundary conditions

$$\zeta \left(R_{tip} \right) = h - \delta \quad (3)$$

and

$$\zeta \left(R \right) = 0 \quad (4)$$

Here the indentation depth δ is the contribution to the normal membrane displacement due to the action of the external load, so that, in the center of the dome ($r = 0$), in absence of AFM indentation, $\zeta(0) = h$.

During the AFM indentation, a spatially uniform deformation depth $h - \delta$ is considered at any distance $r \leq R_{tip}$ (Equation (3)), whereas zero displacement is experienced at the edge (Equation (4)). The numerical solution of Equation (1), together with Equations (2–4), can be pursued in the limits of small and large indentations, leading to $F \approx k\delta$ (linear regime) and $F \approx \alpha\delta^3$ (cubic regime), respectively, with $k \approx \frac{2\pi A_\tau (\Delta p R)^{2/3} E_{2D}^{1/3}}{\log(R/R_{tip})}$ and $\alpha \approx f\left(\nu, \frac{R_{tip}}{R}\right) \frac{E_{2D}}{R^2}$ (A_τ is a tabulated function of Poisson's ratio).[54] It is worth noticing that the linear stiffness k depends on E_{2D}, as well as on the internal pressure p, differently from Schwerin-like models on free-standing membranes.[27,41–43] In the latter, the stretching modulus E_{2D} plays a role only in the

force-indentation response at very large indentation depths (cubic component), whereas k leads the information on material's Poisson ratio ν, radius of the indenter and material's pretension. By using the results on the equilibrium height of highly pressurized blisters,[49,63] $h = A_h \left(\frac{\Delta p R^4}{E_{2D}} \right)^{1/3}$ (A_h is a tabulated function of Poisson's ratio), and combining it with $k \approx \frac{2\pi A_\tau (\Delta p R)^{2/3} E_{2D}^{1/3}}{\log(R/R_{tip})}$, one can demonstrate that the knowledge of both dome's height (before AFM indentation) and stiffness (i.e., slope of loading force curve in the small indentation range) is sufficient for both p and E_{2D} to be inferred. Indeed, under the conditions of 1. small indentation and 2. high pressurization, one can find

$$p \approx \frac{\log\left(\frac{R}{R_{tip}}\right) h k}{2\pi A_h A_\tau R^2} + p_0 \quad (5)$$

and

$$E_{2D} \approx \frac{\log\left(\frac{R}{R_{tip}}\right) A_h^2 R^2 k}{2\pi A_\tau h^2} \quad (6)$$

where $A_h \approx 0.645$ and $A_\tau \approx 0.438$ for $\nu \approx 0.3$, as in the case of MoS_2.[64]

If they are verified, the conditions 1. and 2. are particularly relevant since p and E_{2D} can be expressed independently and thus inferred via indentation experiments. The signature of being in the small indentation regime is given by an approximately constant behavior of the linear stiffness k (i.e., linear
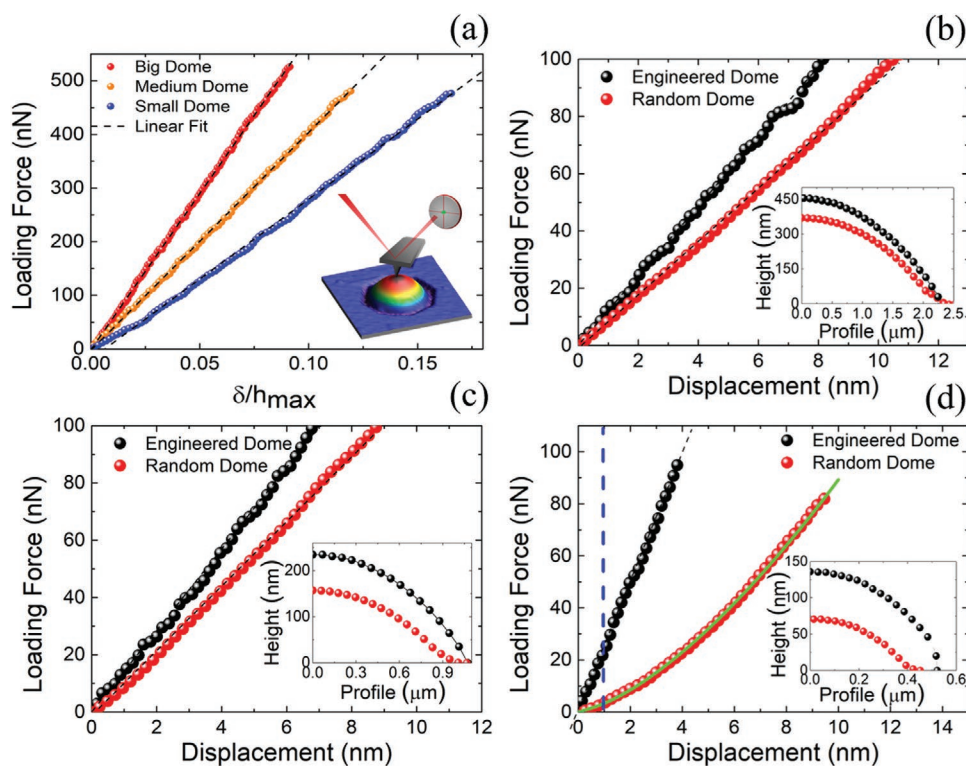
Figure 3. a) Main panel: three typical loading force curves measured on big (red), medium (orange), and small (blue) engineered domes. Black dashed lines are their linear fits. Inset: sketch of the AFM nanoindentation experiments; a loading force is applied through the AFM probe on the top of each selected pressurized dome. b–d) Main panels: loading force curves acquired on big, medium, and small engineered (black dots) and spontaneous (red dots) domes. Insets: Engineered (black) and spontaneous (red) dome's profiles. d) Blue dashed line: threshold depth between linear and nonlinear regime. Green solid line: fit of the loading force curve by Equation (7).

behavior of the loading force curve), whereas the signature of being in the large pressure regime can be extrapolated by studying the dependence of k on the internal pressure (see Note S3 in the Supporting Information).

Figure 3a, which refers to big, medium and small engineered domes, validates the condition of being in the small indentation regime. As sketched in the inset, during a nanoindentation experiment, a loading force is applied along the normal direction after positioning the AFM tip on the top of the dome, and force-distance curves are recorded on each selected membrane. The main panel of Figure 3a shows three typical loading force curves measured on big (red), medium (orange) and small (blue) engineered domes, where the indentation depth δ is normalized to the maximum dome height (h_{max}). A loading force as high as 500 nN is applied, and an indentation depth of about 8%, 12%, and 17%, is reached for big, medium, and small domes, respectively. The black dashed lines represent their linear fits, having relative errors (standard error $\Delta\beta$, divided by the slope β) of $\frac{\Delta\beta}{\beta} =$ 0.05%, 0.06% and 0.19%. These very small values confirm the accuracy of the linear fitting model with respect to the experimental behavior. However, a slight increase of $\frac{\Delta\beta}{\beta}$ is found as the dome's size shrinks, indicating that the nonlinearity arises at lower forces in smaller domes. A similar information is derived in Note S4 in the Supporting Information by studying the slope of the linear fit of the log-log plot of loading force versus indentation depth.

On the other hand, Figure 3b–d compare indentation experiments performed on big (b), medium (c), and small (d) engineered and spontaneous domes (the latter having footprint radii close to the three engineered cases, and differing by 1%, 9% and 16%, respectively), by employing a maximum loading force of 100 nN. In the case of spontaneous domes, we avoided applying higher loads to prevent potentially irreversible situations from occurring, such as the splitting and slipping of the domes. As shown in Note S5 in the Supporting Information, spontaneous domes can move under the AFM solicitation by profiting of a local delamination of the top-most layer at the unconstrained edge. In this scenario, the presence of the HSQ-coating, surrounding the engineered domes, guarantees higher stability under the external load.

Experimental loading force curves measured on engineered and spontaneous domes are plotted in Figure 3b–d as black and red dots, respectively. One can notice that 1) engineered domes are, in general, stiffer than spontaneous ones (the same loading force leads to a higher indentation depth in spontaneous domes), pointing toward a lower pressurization in the latter; 2) in the linear regime, the loading force required to achieve a certain indentation increases as the dome size decreases (which, given the same elastic properties of the MoS_2 membrane, would be qualitatively consistent with an increase of H_2 pressure as $\frac{1}{volume}$); 3) nonlinearity is easily reached in small-size spontaneous domes. The arise of such a nonlinear

behavior indicates that, in the investigated case (spontaneous dome with $h = 69$ nm, $R = 437$ nm, $h/R = 0.157$), the range of indentation depth, achieved by using a loading force of 80 nN $\left(\frac{\delta}{h_{mx}} = 14\%\right)$, covers the intermediate regime (between large and small indentation). Since the transition region between small and large indentation depths is very hard to model analytically, it is a common use to fit such an intermediate regime, with a sum of the asymptotic models obtained in the small and large indentation limits. However, Vella et al. have shown that the out-coming error can be very large, and further increased as the indenter's size shrinks.[54] In the present study, therefore, we have decided to implement a different approach: the loading force curve (red dots in Figure 3d) has been fitted (green line) by the combination of a linear component ($F_L = k\delta$) and a nonlinear component ($F_{NL} = \alpha\delta^{\omega}$), where the exponent ω is found by the optimization of the fitting procedure, both weighted by the Heaviside function $\Theta(\delta - \delta_T)$, with δ_T being the depth threshold between linear and nonlinear regime (blue dashed line in Figure 3d):

$$F(\delta) = k\delta\left(1 - \Theta(\delta - \delta_T)\right) + \left(k\delta_T - \alpha\delta_T + \alpha\delta^{\omega}\right)\left(\Theta(\delta - \delta_T)\right) \quad (7)$$

Our indentation results indicate that a loading force lower than 100 nN is enough to produce a nonlinear response in spontaneously generated domes of medium and small size (with $\delta_T = 1 - 8$ nm), while for the engineered domes the behavior is still linear at least up to 500 nN ($\delta_T > 20$ nm). Such results prove that the condition of small indentation into thin pressurized elastic shells is more insidious than just $\delta_{in} < t$ or $\delta_{in} \ll h_{max}$, where δ_{in} and t are indentation depth and membrane thickness respectively, but the role of the internal pressure has to be taken into account. It is worth noticing that the fitting of force-indentation curves acquired on spontaneous domes, by means of Equation (7), gives $\omega \approx 1.5$, indicating that the cubic behavior of F vs δ is never reached in the presented experiments, with a maximum loading of 100 nN in spontaneous domes and 500 nN in the engineered ones.

A statistical analysis of loading force curves has been carried on by performing nano indentation on 110 engineered domes, as well as, for comparison, on 9 spontaneous domes, having size similar to the engineered ones (due to the randomness in the dome's production process in uncoated flakes, spontaneous domes with the same size as the engineered cases are hard to be found, thus motivating the difference in the number of sampled membranes). We have thus selected and studied the linear regime of the curves relative to each dome to extract an estimate of their internal pressure and of the stretching modulus, via the theoretical expressions derived above (Equations (5) and (6)). Half-black scatters and red stars in **Figure 4** are representative of engineered and spontaneous domes, respectively. Moreover, half-black circles, half-black squares and half-black diamonds will hereinafter indicate small, medium and big curved membranes. Figure 4a shows the behavior of p vs V (dome's volume), as derived by measuring the stiffness k of the loading force curve and employing Equation (5). The internal pressure of both engineered and spontaneous domes decreases as the dome's volume increases (more information on Δp vs $\frac{h^3}{R^4}$ and $\Delta p \frac{R^4}{th^3}$ versus $\frac{h}{t}$, where t is MoS$_2$ monolayer thickness, are reported in Note S6 in the Supporting Information).

The distribution of internal pressure in big, medium and small engineered domes mostly ranges between 1.9 – 2.9 MPa, 3.4 – 4.0 MPa, and 6.5 – 11.7 MPa, respectively. The larger dispersion of pressure values in small membranes is fully accounted by the stiffer variation of the function $p \propto \frac{1}{V}$ as the volume approaches zero. Moreover, as expected from the loading force curve behavior of Figure 3, the pressure measured in spontaneous domes is generally lower than in the engineered ones, ranging from 1.2 to 9.3 MPa, as a function of the dome's volume. Table 1 compares one by one the pressure measured in the engineered and spontaneous domes given almost the same footprint radius in the first case, and almost the same volume in the second. In both comparisons, engineered membranes support higher internal pressure. Given the same volume, Table 2 lists the number N of molecules inside each dome (and the relative moles n) as calculated by employing the van der Waals equation for the real gases $\left[P + a\left(\frac{n}{V}\right)^2\right]\left(\frac{V}{n} - b\right) = RT$, where $a = 0.2419 \frac{atmL^2}{mol^2}$ and $b = 0.02651 \frac{L}{mol}$ are the van der Waals constants for H$_2$ gas,[65] $R = 0.0821 \frac{atmL}{molK}$ and $N = nN_A$ ($N_A = 6.022 \times 10^{23}$ is the Avogadro number). The correction to N (or n), coming from using the van der Waals equation rather than the ideal gas law, is less than 10%, given the low compressibility of H$_2$ gas.

Figure 4b shows the results of the analysis of the linear component of the loading force curves in terms of 2D and 3D Young's modulus, E_{2D} (left scale) and $Y = \frac{E_{2D}}{t}$ (right scale—where $t = 0.65$ nm is the monolayer thickness), respectively. Here, the yellow patterned region highlights the range of Young's modulus values reported in literature [27,41,42,64] for MoS$_2$ monolayers produced by using different approaches. Our results fully lie in the expected range. It is worth noticing that only small size domes exhibit occurrences of lower E_{2D} (Y), both in the engineered and spontaneous cases. We infer that such a result can be affected by the finite size of the indenter. Indeed, even with the smallest tip used ($R_{tip} \approx 40$ nm), the ratio $\frac{R_{tip}}{R}$ on the smallest domes is ≈0.1, leading to some spurious effects, such as an enhanced probability of off-center indentation, with consequent asymmetric tip-dome contact area during the loading procedure. Besides such a side effect, the scattering of E_{2D} (Y) values can be likely attributed to the sampling of different flakes, which may intrinsically have slightly different stretching moduli, due for example to the (random) density of defects created during the mechanical exfoliation.

In the main panel of Figure 4c we evaluate the 2D and 3D in-plane stress of the bulged MoS$_2$ membranes, as $\sigma_{2D} = \frac{pR^2}{2h}$ (from the Young-Laplace law) and $\sigma_{3D} = \frac{\sigma_{2D}}{t}$, respectively. The blue dashed line identifies the maximum stress supported by the MoS$_2$ membrane before rupture ($\sigma_{2D} = 15.5 \frac{N}{m}, \sigma_{3D} = 23.8$ GPa), as predicted by first-principle calculations.[26] All our domes lie beneath this threshold, with the engineered membranes being almost at the stress limit. Moreover, the inset of Figure 4c shows the MoS$_2$ membrane strain, as evaluated by using $\varepsilon = \frac{\sigma_{2D}}{E_{2D}}$. In agreement with,[40] all the spontaneous domes have almost the same ε, whereas overall the engineered domes support an higher strain. It is worth mentioning that when σ approaches

**ADVANCED
SCIENCE NEWS**

www.advancedsciencenews.com

**ADVANCED
MATERIALS
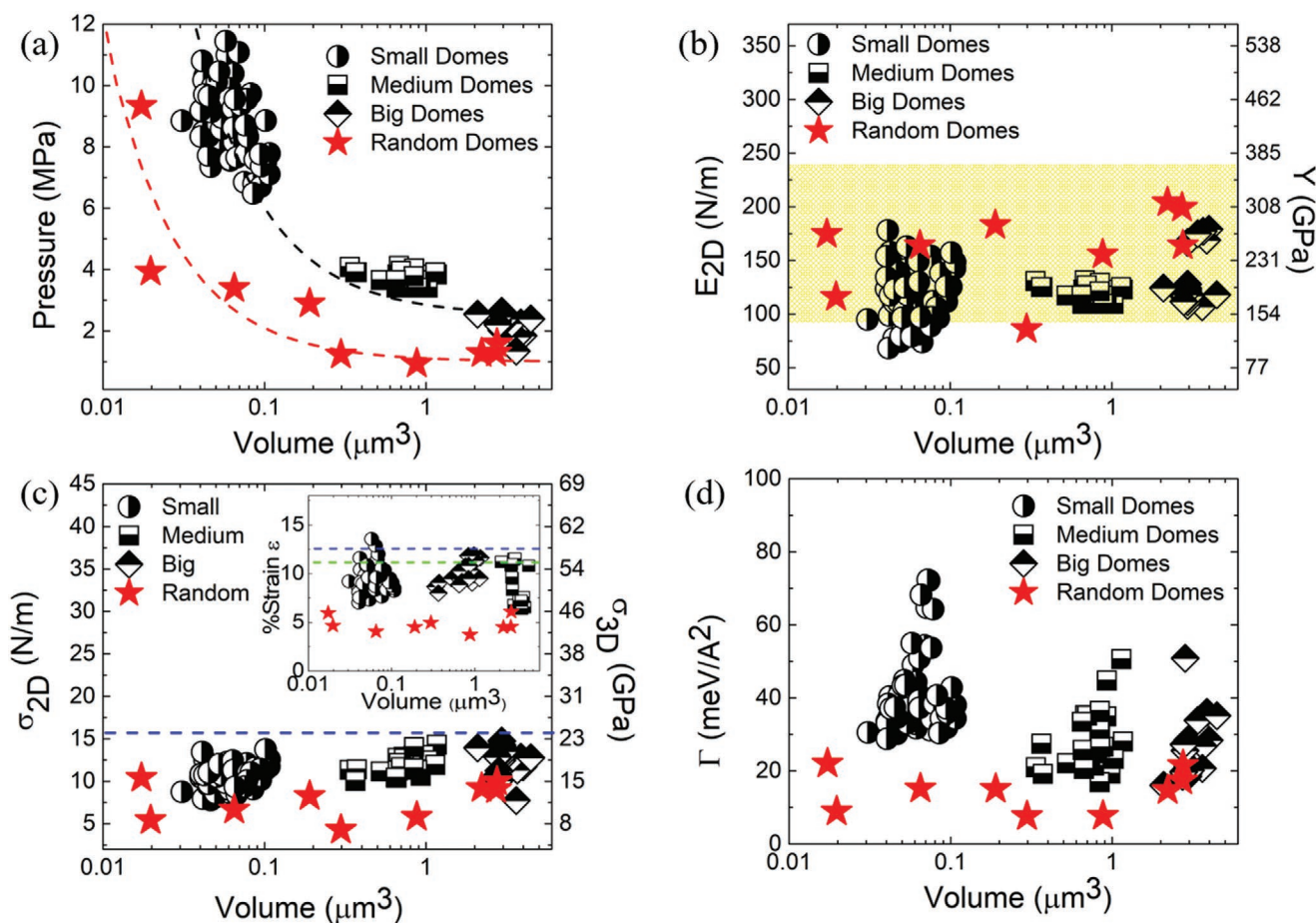INTERFACES**

www.advmatinterfaces.de

Figure 4. a) Main plot: H_2 pressure versus dome's volume for engineered (half-black scatters) and spontaneous (red stars) domes. Black and red dashed lines work as a guide for the eye to follow the behavior of p versus V. b) Stretching modulus E_{2D} versus dome's volume for engineered (half-black scatters) and spontaneous (red stars) domes. The yellow area highlights the range of E_{2D} values reported in literature for MoS_2 monolayer.[27,41,42,64] c) Main plot: stress versus dome's volume for engineered (half-black scatters) and spontaneous (red stars) domes. Blue dashed line: critical stress value at the failure point.[26,27] Inset: strain versus dome's volume for engineered (half-black scatters) and spontaneous (red stars) domes. Green dashed line: Griffith's strain limit $\frac{\sigma_{max}}{Y} \approx \frac{1}{9}$. Blue dashed line: MoS_2 strain limit $\frac{\sigma_{max}}{Y} \approx \frac{1}{8}$. d) Adhesion energy versus dome's volume for engineered (half-black scatters) and spontaneous (red stars) domes.

the critical value (as in the engineered case), the stress–strain relationship is no longer linear, and the expression $\varepsilon = \frac{\sigma_{2D}}{E_{2D}}$ can only give an approximate estimate of ε. As a matter of fact,

Table 1. Comparison of internal pressure between engineered and spontaneous domes with similar footprint radius (first raw) and similar volume (second raw).

	Engineered		Spontaneous	
	Radius [µm]	Pressure [MPa]	Radius [µm]	Pressure [MPa]
Big	2.1	2.4	2.2	1.4
Medium	1.04	4.1	0.9	2.8
Small	0.47	9.1	0.43	4.4
	Volume [µm³]	Pressure [MPa]	Volume [µm³]	Pressure [MPa]
Big	2.2	2.4	2.2	1.1
Medium	0.9	3.8	0.9	0.9
Small	0.047	7.4	0.047	3.3

the strain measured here reached slightly higher values than those estimated via theoretical models (such as Hencky's model [66] and finite element method calculations [39–40]): spontaneous domes support an average strain of $(4.8 \pm 1.2)\%$, to be compared to an expected value of 3.5 – 4.7%, whereas a strain in the range 6% – 13%, 8% – 12% and 6.4% – 11.5% is measured in small,

Table 2. Number of particles (and moles) per each size engineered and spontaneous dome, calculated by employing the van der Waals equation for real gases.

	Engineered	Spontaneous
Big	1.3×10^9	5.8×10^8
	2.1×10^{-15} mol	9.6×10^{-16} mol
Medium	8.0×10^8	1.9×10^8
	1.3×10^{-15} mol	3.2×10^{-16} mol
Small	8.0×10^7	3.7×10^7
	1.3×10^{-16} mol	6.1×10^{-17} mol

ADVANCED
SCIENCE NEWS
www.advancedsciencenews.com

ADVANCED
MATERIALS
INTERFACES
www.advmatinterfaces.de

medium and big domes, to be compared to expected values of 5 – 11%, 5 – 8% and 5 – 7%, respectively. A slight over-estimate of the membrane strain is fully expected when using the AFM loading experiments as a measurement technique. Indeed, the nanoindentation itself introduces an additional local strain, decreasing as $\left(\frac{1}{r}\right)^{2/3}$ from the loading point at $r = 0$.[47,67] With a maximum applied load $F_{max} = 100$ nN, the strain imposed by a spherical probe indenting a linearly elastic membrane is $\varepsilon_{AFM} = \sqrt{\frac{F_{max}}{4\pi E_{2D} R_{tip}}}$,[27] that in our case results in $\varepsilon_{AFM} = 2\% - 5\%$, depending on stretching modulus value and on the tip used. Even though the linearly elastic regime is strictly guaranteed only in the case of spontaneous domes—given the value of the membrane stress—this amount, added to the pre-existing strain of the membrane, accounts for an over-estimate of the measured ε. Finally, green and blue dashed lines in the inset represent the Griffith ideal strength limit $\left(\frac{\sigma_{max}}{Y} \approx \frac{1}{9}\right)$—the maximum stress any material is predicted to withstand, given its Y—and the DFT expectation for single-layer MoS$_2$, $\frac{\sigma_{max}}{Y} \approx \frac{1}{8}$,[28] further confirming that engineered domes are close to the limit of the supported stress/strain.

Within the framework of the membrane model, the simultaneous knowledge of the equilibrium dome's size (radius R and height h) and the stretching modulus (E_{2D}) leads to the estimate of the MoS$_2$ adhesion energy: $\Gamma = \frac{E_{2D} h^4}{\varphi R^4}$.[52,53] The constant pre-factor φ, which relates the aspect ratio of the domes (or ultimately the strain of the membrane) to the ratio of adhesion energy to stretching modulus, has been shown to assume different values depending on the coupling between the material and substrate, in the two opposite limits of strong $\left(\varphi = \frac{24(1-v)}{5(7-v)}\right)$ and weak $\left(\varphi = \frac{6}{5}\right)$ shear.[53] In a typical modelling of blisters in 2D materials, the blister's edges are always assumed to be fully clamped (strong shear) due to the adhesion with the supporting substrate outside the boundary. This assumption may be sometimes quite far from reality, indeed the atomically smooth surfaces of 2D materials make interfacial sliding particularly easy, giving rise to the phenomenon of superlubrification (near-zero friction) when a 2D material sits on atomically flat substrates, including itself (weak shear).[68] Note S7 in the Supporting Information provides the evidence, based on Raman results, that a strong-shear coupling sets up both in spontaneus and engineered domes. In Figure 4d we show the values of Γ for each investigated dome. Interestingly, the adhesion energy in spontaneous domes ranges between $\Gamma_{sp} = 7.6 - 22$ meV/Å^2, very close to previous experimental results,[29,57,69] and to the values theoretically predicted in.[70] It's worth noticing that the excellent agreement between the adhesion energy estimated here and in [29] is consistent with the investigation of domes with the same aspect ratio $\left(\frac{h}{R} \approx 0.16\right)$. On the other hand, higher values of Γ_{eng} are recorded in engineered domes, with a further increasing trend when the dome's size shrinks. The value of Γ_{eng} in big and medium membranes ranges almost in the same interval $20 - 40$ meV/Å^2 (with only few outliers at lower and higher values), whereas a continuous distribution of Γ_{eng},

between 28– 73 meV/Å^2, is measured in small domes. In general, the relationship between adhesion energy Γ, exfoliation energy Γ_{ex}, and surface energy Γ_{surf} is $\Gamma_{ex} \approx \Gamma \approx 2\Gamma_{surf}$.[70] Such a relation fully describes the spontaneous case, Γ_{sp}, whereas, in the engineered case, the patterning contributes to an "effective" adhesion energy, Γ_{eng}. The value of Γ_{eng} is thus not only affected by the MoS$_2$-MoS$_2$ surface energy but also by the presence of the superimposed HSQ mask as well as by the size of the openings. Indeed, the presence of the mask translates into the formation of domes with aspect ratios $\frac{h}{R}$ exceeding the universal value, and spanning over a wide range, in between 0.15 and 0.31,[40] thus resulting in an "effective" Γ_{eng}, higher than Γ_{sp}, given the same Γ_{surf}. The superimposed mask on one side allows the exfoliation to happen only in specific locations, i.e., the openings in the HSQ-layer, and on the other side acts as a spatial constraint against the exfoliation of the MoS$_2$ monolayer toward the formation of the spherical membrane. In this framework, reducing the portion of surface area participating in the hydrogen production process (by reducing the size of the opening), increases the effect of the clamped boundary against the lift-up of the topmost MoS$_2$ layer.

3. Conclusion

In this paper we have demonstrated an innovative approach for measuring the internal pressure, stretching modulus, membrane stress/strain, and adhesion energy of 2D material blisters, by performing AFM nanoindentation experiments and by interpreting the results in the membrane limit of the Föppl–von Karman equation.[53,54] We tested H$_2$-filled MoS$_2$ domes produced by the local exfoliation of the topmost S-Mo-S layers, due to low-energy proton irradiation of bulk flakes. We compared the properties of MoS$_2$ domes in two different cases: 1) spontaneous generation (random spatial distribution of domes of random size); 2) engineered creation, i.e., spatially controlled nucleation (uniform distribution of the dome's size within a regular pattern) for three pattern periodicities and opening sizes. This second method has been optimized on purpose to create structures with remarkably different characteristics, such as higher internal pressure and fully clamped boundaries. Our AFM experiments, supported by theoretical models,[53,54] have led to the quantification of the H$_2$ pressure inside each selected membrane, confirming that the engineered domes are subjected to higher pressurization, compared to the spontaneous ones, as expected by their higher aspect ratio (or strain), as also discussed elsewhere.[40] Moreover, we have shown that the inner pressure further increases by reducing the dome's volume. We believe that the exact knowledge of H$_2$ pressure (or ultimately the knowledge of the number of gas moles confined in the domes), together with the possibility of fabricating a controlled distribution of equally sized domes, can have a strong impact in the field of hydrogen storage and extraction, for applications requiring the on-demand release of well-known, extremely small amounts of hydrogen gas.

Moreover, from the indentation experiments we were able to evaluate the stretching modulus of MoS$_2$ as $E_{2D} = (150 \pm 36)$ N/m, which can be converted into the 3D Young's modulus

value by dividing E_{2D} by the interlayer distance (0.65 nm), resulting in: $Y = (231 \pm 55)$ GPa, in good agreement with previously reported values.[27,41,42,64]

Furthermore, we have used the Young-Laplace law to evaluate the in-plane stress of the bulged membranes, and their relative strain. Our results indicate that 1. engineered domes always support higher stress/strain, compared to the spontaneous case, and 2. stress/strain values in engineered membranes, further strained by the nanoindentation procedure, are close to the breaking point. This remarkable result suggests the engineered formation of domes via proton-irradiation to be an ideal method for subjecting 2D materials to extremely high strains.

Finally, we have evaluated the adhesion energy (or exfoliation energy, i.e., the cost of removing a single layer from the surface of the bulk compound) in the limit of clamped and fully bonded interface (strong shear). Our results indicate an increase of the effective exfoliation energy when MoS_2 flakes are coated by the HSQ layer. Moreover, the exfoliation energy is shown to be further enhanced when the opening size shrinks, interpreted as a consequence of the higher resistance of the clamped boundary against the delamination of topmost MoS_2 layers.

4. Experimental Section

Sample Preparation and Proton Irradiation: Thick MoS_2 flakes (hundreds of layers) were first mechanically exfoliated onto Si/SiO₂ substrates. Part of the substrates was then coated with HSQ masks and subjected to electron beam lithography, as detailed in the next section. With this procedure, both coated and uncoated flakes were present on a same sample. The samples were subsequently ion-irradiated with a Kaufman source.[39] To perform irradiation, the sample was mounted on a metallic holder so as to be grounded. The holder was placed into a vacuum chamber, which was brought to a base pressure $<1 \times 10^{-6}$ mbar, and the temperature was raised to a value in the range 120–150°C. Hydrogen ions were obtained in an ionization chamber and accelerated by a system of grids, thus irradiating the sample with a ion beam with energy in the range 10–20 eV. The samples were irradiated with a total dose in the range $6-7 \times 10^{16}$ protons/cm².

Electron-Beam Lithography Patterning: The engineered formation of MoS_2 domes was achieved via the fabrication of H-opaque masks, treated by means of electron-beam lithography (EBL, Vistec EPBG 5HR system working at 100 kV). The engineering procedure was as follows:[39] a hydrogen silsesquioxane (HSQ) negative-tone e-beam resist was spun onto the sample surface. EBL was then performed to get octagonal openings of predetermined dimensions and with the desired ordering on the HSQ layer. An electron dose of 300 µC cm⁻² and an aqueous development solution of tetramethyl ammonium hydroxide at 2.4% were used for the patterning of the HSQ masks. In order to make the resist act as a constraint during the dome formation process, a resist thickness ≥50 nm was employed. Moreover, being the HSQ a negative-tone resist, only the area irradiated with the electron beam was subjected to a hardening during the EBL process. As a consequence, only the electron-irradiated area finally remains on the sample, as the unexposed HSQ dissolves in the developer.

Atomic Force Microscopy Measurements: AFM images have been acquired by using a JPK Nanowizard III, equipped with Vortex electronics, in the standard tapping mode technique, by using a LTESP Si probe (from Bruker). The measurement of the elastic properties has been achieved by exerting a loading force of 80–500 nN at the center of the pressurized membrane to perform nanoindentation AFM experiments. The indentation depth δ was determined as $\delta = \Delta z_{piezo} - \Delta z_{tip}$, where Δz_{piezo} was the displacement of the AFM piezotube and Δz_{tip} was the deflection of the cantilever, measured by the photodiode. In order to

preserve the tip's shape and size, the cantilever characterization has been carried out, prior to performing the indentation, by employing the contact-free method,[72] which does not require preceding force-distance curve acquisition on a hard material to determine cantilever sensitivity, although it only applies to rectangular cantilevers. The knowledge of the cantilever's geometrical dimensions (length and width) as well as of the physical properties of the environment/medium (density and viscosity) where the measurements are performed is mandatory to derive reliable values of the spring constant s and deflection sensitivity δ_c, besides resonance frequency f_0 and quality factor, by employing thermal noise measurement. The presented experiments have been performed at room temperature under ambient conditions (density $\approx$ 1.185 kg m⁻³ and viscosity $\approx$ 18.37 µPa x sec) and by using rectangular cantilevers of 225 µm in length and 35 µm in width, having in average $\delta_c \approx 40$ nm/V and $s \approx 50$ N/m. s and δ_c have been tested afterward, by employing the standard contact-based method at the end of each measurement run, on a hard substrate (e.g., Si/SiO₂), confirming the results of the contact-free procedure. The curvature radius of the used probes has been tested before and after each indentation experiment, through the topographic imaging of a sharp step of known height a,[73] resulting in $40 - 100$ nm. A single atomic step of freshly cleaved muscovite mica or highly oriented pyrolytic graphite (HOPG) was chosen to be imaged and R_{tip} was extracted from its observed width w, which was caused by the convolution with the finite probe, $R_{tip} = \frac{a^2 + w^2}{2a}$. This procedure was tested on several new tips of distinct size, ranging from tens to hundreds of nm, and a high consistence was found between the measure of R_{tip} and the values declared by the factory.

Such values of R_{tip}, compared to the indentation depth, in the small indentation regime ($\delta \leq 10$ nm), ensure a negligible change in contact area during the indentation procedure ($\frac{A_c^* - A_c}{A_c} < 5\%$, where $A_c = \pi R_{tip}^2$ and $A_c^*(\delta) = \pi(R_{tip}^2 + \delta^2)$).

All the data were analyzed by using WsXM, Scanning Probe Image Processor (SPIP), Origin and Mathematica.

Conflict of Interest

The authors declare no conflict of interest.

[1] X. Li, H. Zhu, *J. Materiomics* **2015**, *1*, 33.
[2] K. F. Mak, C. Lee, J. Hone, J. Shan, T. F. Heinz, *Phys. Rev. Lett.* **2010**, *105*, 136805.

**ADVANCED
SCIENCE NEWS**

www.advancedsciencenews.com

**ADVANCED
MATERIALS
INTERFACES**

www.advmatinterfaces.de

[3] B. Radisavljevic, A. Radenovic, J. Brivio, V. Giacometti, A. Kis, *Nat. Nanotechnol.* **2011**, *6*, 147.

[4] O. Lopez-Sanchez, D. Lembke, M. Kayci, A. Radenovic, A. Kis, *Nat. Nanotechnol.* **2013**, *8*, 497.

[5] H. Li, Z. Yin, Q. He, H. Li, X. Huang, G. Lu, D. W. Fam, A. I. Tok, Q. Zhang, H. Zhang, *Small* **2012**, *8*, 63.

[6] W. Jin, P. C. Yeh, N. Zaki, D. Zhang, J. T. Sadowski, A. Al-Mahboob, A. M. van der Zande, D. A. Chenet, J. I. Dadap, I. P. Herman, P. Sutter, J. Hone Jr., R. M. Osgood, *Phys. Rev. Lett.* **2013**, *111*, 106801.

[7] H. P. Komsa, A. V. Krasheninnikov, *Phys. Rev. B* **2012**, *86*, 241201.

[8] D. J. Trainer, A. V. Putilov, C. Di Giorgio, T. Saari, B. Wang, M. Wolak, R. U. Chandrasena, C. Lane, T. R. Chang, H. T. Jeng, H. Lin, F. Kronast, A. X. Gray, X. X. Xi, J. Nieminen, A. Bansil, M. Iavarone, *Sci. Rep.* **2017**, *7*, 40559.

[9] A. Castellanos-Gomez, R. Roldán, E. Cappelluti, M. Buscema, F. Guinea, H. S. J. van der Zant, G. A. Steele, *Nano Lett.* **2013**, *13*, 5361.

[10] H. J. Conley, B. Wang, J. I. Ziegler Jr., R. F. Haglund, S. T. Pantelides, K. I. Bolotin, *Nano Lett.* **2013**, *13*, 3626.

[11] A. V. Tyurnina, D. A. Bandurin, E. Khestanova, V. G. Kravets, M. Koperski, F. Guinea, A. N. Grigorenko, A. K. Geim, I. V. Grigorieva, *ACS Photonics* **2019**, *6*, 516.

[12] D. J. Trainer, Y. Zhang, F. Bobba, X. X. Xi, S. W. Hla, M. Iavarone, *ACS Nano* **2019**, *13*, 8284.

[13] E. Blundo, M. Felici, T. Yildirim, G. Pettinari, D. Tedeschi, A. Miriametro, B. Liu, W. Ma, Y. Lu, A. Polimeni, *Phys. Rev. Res.* **2020**, *2*, 012024(R).

[14] J. Fuhr, A. Saúl, J. Sofo, *Phys. Rev. Lett.* **2004**, *92*, 026802.

[15] W. Zhou, X. Zou, S. Najmaei, Z. Liu, Y. Shi, J. Kong, J. Lou, P. M. Ajayan, B. I. Yakobson, J. C. Idrobo, *Nano Lett.* **2013**, *13*, 2615.

[16] Q. Yue, S. Chang, S. Qin, J. Li, *Phys. Lett. A* **2013**, *377*, 1362.

[17] M. Precner, T. Polakovic, Q. Qiao, Y. Zhu, D. Trainer, A. Putilov, C. Di Giorgio, I. Cone, X. Xi, M. Iavarone, G. Karapetrov, *Sci. Rep.* **2018**, *8*, 6724.

[18] M. Precner, T. Polakovic, D. Trainer, A. Putilov, C. Di Giorgio, I. Cone, X. Xi, M. Iavarone, G. Karapetrov, *AIP Conf. Proc.* **2018**, *1*, 2005.

[19] R. B. Somoano, A. Rembaum, *Phys. Rev. Lett.* **1971**, *27*, 402.

[20] J. A. Woollam, R. B. Somoano, *Phys. Rev. B* **1976**, *13*, 3843.

[21] R. Zhang, I.-L. Tsai, J. Chapman, E. Khestanova, J. Waters, I. V. Grigorieva, *Nano Lett.* **2016**, *16*, 629.

[22] J. Martinez-Castro, D. Mauro, A. Pásztor, I. Gutiérrez-Lezama, A. Scarfato, A. F. Morpurgo, C. Renner, *Nano Lett.* **2018**, *18*, 6696.

[23] D. J. Trainer, B. K. Wang, F. Bobba, N. Samuelson, X. Xi, J. Zasadzinski, J. Nieminen, A. Bansil, M. Iavarone, *ACS Nano* **2020**, *14*, 2718.

[24] Z. Chi, X. Chen, F. Yen, F. Peng, Y. Zhou, J. Zhu, Y. Zhang, X. Liu, C. Lin, S. Chu, Y. Li, J. Zhao, T. Kagayama, Y. Ma, Z. Yang, *Phys. Rev. Lett.* **2018**, *120*, 037002.

[25] T. Dvir, M. Aprili, C. H. L. Quay, H. Steinberg, *Nano Lett.* **2018**, *18*, 7845.

[26] T. Li, *Phys. Rev. B* **2012**, *85*, 235407.

[27] R. C. Cooper, C. Lee, C. A. Marianetti, X. Wei, J. Hone, J. W. Kysa, *Phys. Rev. B* **2013**, *87*, 035423.

[28] S. Bertolazzi, J. Brivio, A. Kis, *ACS Nano* **2011**, *5*, 9703.

[29] E. Khestanova, F. Guinea, L. Fumagalli, A. K. Geim, I. V. Grigorieva, *Nat. Commun.* **2016**, *7*, 12587.

[30] T. Georgiou, L. Britnell, P. Blake, R. V. Gorbachev, A. Gholinia, A. K. Geim, C. Casiraghi, K. S. Novoselov, *Appl. Phys. Lett.* **2011**, *99*, 093103.

[31] A. V. Kretinin, Y. Cao, G. L. Y. u. J. S. Tu, R. Jalil, K. S. Novoselov, S. J. Haigh, A. Gholinia, A. Mishchenko, M. Lozada, T. Georgiou, C. R. Woods, F. Withers, P. Blake, G. Eda, A. Wirsig, C. Hucho, K. Watanabe, T. Taniguchi, A. K. Geim, R. V. Gorbachev, *Nano Lett.* **2014**, *14*, 3270.

[32] L. Xie, L. Jiao, H. Dai, *J. Am. Chem. Soc.* **2010**, *132*, 14751.

[33] S. Xiao, P. Xiao, X. Zhang, D. Yan, X. Gu, F. Qin, Z. Ni, Z. J. Han, K. Ostrikov, *Sci. Rep.* **2016**, *6*, 19945.

[34] A. Malesevic, R. Vitchev, K. Schouteden, A. Volodin, L. Zhang, G. Van Tendeloo, A. Vanhulsel, C. Van Haesendonck, *Nanotechnology* **2008**, *19*, 305604.

[35] J. Kim, M. Ishihara, Y. Koga, K. Tsugawa, M. Hasegawa, S. Iijima, *Appl. Phys. Lett.* **2011**, *98*, 091502.

[36] L. He, H. Wang, L. Chen, X. Wang, H. Xie, C. Jiang, C. Li, K. Elibol, J. Meyer, K. Watanabe, T. Taniguchi, Z. Wu, W. Wang, Z. Ni, X. Miao, C. Zhang, D. Zhang, H. Wang, X. Xie, *Nat. Commun.* **2019**, *10*, 2815.

[37] E. Stolyarova, D. Stolyarov, K. Bolotin, S. Ryu, L. Liu, K. T. Rim, M. Klima, M. Hybertsen, I. Pogorelsky, I. Pavlishin, K. Kusche, J. Hone, P. Kim, H. L. Stormer, V. Yakimenko, G. Flynn, *Nano Lett.* **2009**, *9*, 332.

[38] D. C. Elias, R. R. Nair, T. M. G. Mohiuddin, S. V. Morozov, P. Blake, M. P. Halsall, A. C. Ferrari, D. W. Boukhvalov, M. I. Katsnelson, A. K. Gei, K. S. Novoselov, *Science* **2009**, *323*, 610.

[39] D. Tedeschi, E. Blundo, M. Felici, G. Pettinari, B. Liu, T. Yildirim, E. Petroni, C. Zhang, Y. Zhu, S. Sennato, Y. Lu, A. Polimeni, *Adv. Mater.* **2019**, *31*, 1903795.

[40] E. Blundo, C. Di Giorgio, G. Pettinari, T. Yildirim, M. Felici, Y. Lu, F. Bobba, A. Polimeni, *Adv. Mater. Interfaces* **2020**, *7*, 2000621.

[41] A. Castellanos-Gomez, M. Poot, G. A. Steele, H. van der Zant, N. Agrait, G. Rubio-Bollinger, *Adv. Mater.* **2012**, *24*, 772.

[42] K. Liu, Q. Yan, M. Chen, W. Fan, Y. Sun, J. Suh, D. Fu, S. Lee, J. Zhou, S. Tongay, J. Ji, J. B. Neaton, J. Wu, *Nano Lett.* **2014**, *14*, 5097.

[43] C. Lee, X. Wei, J. W. Kysar, J. Hone, *Science* **2008**, *321*, 385.

[44] G. López-Polín, C. Gómez-Navarro, V. Parente, F. Guinea, M. I. Katsnelson, F. Pérez-Murano, J. Gómez-Herrero, *Nat. Phys.* **2015**, *11*, 26.

[45] X. Wei, Z. Meng, L. Ruiz, W. Xia, C. Lee, J. W. Kysar, J. C. Hone, S. Keten, H. D. Espinosa, *ACS Nano* **2016**, *10*, 1820.

[46] Y. Li, C. Yu, Y. Gan, P. Jiang, J. Yu, Y. Ou, D. F. Zou, C. Huang, J. Wang, T. Jia, Q. Luo, X. F. Yu, H. Zhao, C. F. Gao, J. Li, *npj Comput. Mater.* **2018**, *4*, 49.

[47] K. Elibol, B. C. Bayer, S. Hummel, J. Kotakoski, G. Argentero, J. C. Meyer, *Sci. Rep.* **2016**, *6*, 28485.

[48] J. S. Bunch, S. S. Verbridge, J. S. Alden, A. M. van der Zande, J. M. Parpia, H. G. Craighead, P. L. McEuen, *Nano Lett.* **2008**, *8*, 2458.

[49] S. P. Koenig, N. G. Boddeti, M. L. Dunn, J. S. Bunch, *Nat. Nanotechnol.* **2011**, *6*, 543.

[50] Z. Zong, C. L. Chen, M. R. Dokmeci, K. T. Wan, *J. Appl. Phys.* **2010**, *107*, 026104.

[51] K. Yue, W. Gao, R. Huang, K. M. Liechti, *J. Appl. Phys.* **2012**, *112*, 083512.

[52] P. Wang, W. Gao, Z. Cao, K. M. Liechti, R. Huang, *J. Appl. Mech.* **2013**, *80*, 040905.

[53] Z. Dai, Y. Hou, D. A. Sanchez, G. Wang, C. J. Brennan, Z. Zhang, L. Liu, N. Lu, *Phys. Rev. Lett.* **2018**, *121*, 266101.

[54] D. Vella, B. Davidovitchb, *Soft Matter* **2017**, *13*, 2264.

[55] A. Pacheco-Sanjuán, R. Batra, *Int. J. Mech. Sci.* **2019**, *163*, 105154.

[56] C. Davini, A. Favata, R. Paroni, *Int. J. Nonlinear Mech.* **2019**, *116*, 281.

[57] B. H. Tan, J. Zhang, J. Jin, C. H. Ooi, Y. He, R. Zhou, K. Ostrikov, N. T. Nguyen, H. An, *Nano Lett.* **2020**, *20*, 3478.

[58] S. H. Petrosko, R. Johnson, H. White, C. A. Mirkin, *J. Am. Chem. Soc.* **2016**, *138*, 7443.

[59] W. H. Roos, R. Bruinsma, G. J. L. Wuite, *Nat. Phys.* **2010**, *6*, 733.

[60] D. Vella, A. Ajdari, A. Vaziri, A. Boudaoud, *J. R. Soc. Interface* **2012**, *9*, 448.

[61] E. S. Ventsel, T. Krauthammer, *Appl. Mech. Rev.* **2001**, *55*, B72.

[62] L. D. Landau, E. M. Lifshitz, *Theory of Elasticity*, Vol. *7*, 3rd ed., Butterworth Heinemann, Oxford **1986**.

[63] H. M. Jensen, *Eng. Fract. Mech.* **1991**, *40*, 475.

[64] D. Akinwande, C. J. Brennan, J. S. Bunch, P. Egberts, J. R. Felts, H. Gao, R. Huang, J.-S. Kim, T. Li, Y. Li, K. M. Liechti, N. Lu, H. S. Park, E. J. Reed, P. Wang, B. I. Yakobson, T. Zhang, Y.-W. Zhang, Y. Zhou, Y. Zhu, *Extreme Mech. Lett.* **2017**, *13*, 42.

[65] The Engineering ToolBox, https://www.engineeringtoolbox.com/non-ideal-gas-van-der-Waals-equation-constants-gas-law-d_1969.html.

[66] W. B. Fichter, *NASA Technical Paper* **1997**.

[67] R. Beams, L. G. Cançado, A. Jorio, A. N. Vamivakas, L. Novotny, *Nanotechnology* **2015**, *26*, 175702.

[68] O. Hod, M. Urbakh, D. Naveh, M. Bar-Sadan, A. Ismach, *Adv. Mater.* **2018**, *30*, 1706581.

[69] D. A. Sanchez, Z. Dai, P. Wang, A. Cantu-Chavez, C. J. Brennan, R. Huang, N. Lu, *Proc. Natl. Acad. Sci. USA* **2018**, *115*, 7889.

[70] T. Bjorkman, A. Gulans, A. V. Krasheninnikov, R. M. Nieminen, *Phys. Rev. Lett.* **2012**, *108*, 235502.

[71] J. Felton, E. Blundo, S. Ling, J. Glover, Z. R. Kudrynskyi, O. Makarovsky, Z. D. Kovalyuk, E. Besley, G. Walker, A. Polimeni, A. Patané, *Molecules* **2020**, *25*, 2526.

[72] J. E. Sader, *Rev. Sci. Instrum.* **1999**, *70*, 3967.

[73] S. Xu, N. A. Amro, G. Y. Liu, *Appl. Surf. Sci.* **2001**, *175–176*, 649.

[74] D. Lloyd, X. Liu, J. W. Christopher, L. Cantley, A. Wadehra, B. L. Kim, B. B. Goldberg, A. K. Swan, J. S. Bunch, *Nano Lett.* **2016**, *16*, 5836.